

# RAIDER: Rapid, anatomy-independent deep learning-based chemical shift-encoded MRI

Timothy JP Bray<sup>1,2,3</sup>  | Giulio V Minore<sup>3</sup>  | Alan Bainbridge<sup>1,4</sup>  | Stuart A Taylor<sup>1,2</sup>  | Margaret A Hall-Craggs<sup>1,2</sup>  | Hui Zhang<sup>3</sup> 

<sup>1</sup>Centre for Medical Imaging, University College London, London, United Kingdom

<sup>2</sup>Department of Imaging, University College London Hospital, London, United Kingdom

<sup>3</sup>Department of Computer Science and Centre for Medical Image Computing, University College London, London, United Kingdom

<sup>4</sup>Department of Medical Physics, University College London Hospital, London, United Kingdom

## Correspondence

Timothy J.P. Bray, Centre for Medical Imaging, University College London, 2nd Floor Charles Bell House, 43-45 Foley Street, W1W 7TS. Email: t.bray@ucl.ac.uk

## Funding Information

This work was supported by The National Institute for Health Research Biomedical Research Centre; grant BRC1121/HEI/TB/110410. Timothy Bray receives personal support from the National Institute for Health Research Biomedical Research Centre. Giulio Minore is supported by the EPSRC-funded UCL Centre for Doctoral Training in Intelligent, Integrated Imaging in Healthcare (i4health) (EP/S021930/1) and the Department of Health's NIHR-funded Biomedical Research Centre at University College London Hospitals.

**Purpose:** Despite recent advances, chemical shift-encoded MRI (CSE-MRI) remains a challenging problem and many algorithms are computationally expensive, leading to interest in deep learning-based methods. However, initial attempts have used convolutional neural networks (CNNs), which are limited by data requirements, poor generalisability across different anatomies ('anatomy-dependence') and training time. To address these limitations, we propose RAIDER, a method for rapid, anatomy-independent deep learning-based CSE-MRI.

**Theory and Methods:** RAIDER uses two multilayer perceptrons (MLPs), each trained separately with simulated single-voxel data, thus avoiding the degeneracy encountered during training when using only one network. During inference, the solution from one of the two networks is chosen based on likelihood. Performance and speed are investigated in a series of simulation experiments, in phantoms and *in vivo*.

**Results:** RAIDER is approximately 700 times faster than conventional fitting, taking  $14\mu\text{s}$  per voxel rather than 10ms, and offers performance similar to that of conventional fitting. It produces accurate fat fraction measurements in phantoms and *in vivo* images with different anatomies, despite having been trained only on simulation data.

**Conclusion:** RAIDER resolves the problems posed by degeneracy, avoids the training data requirements of CNN-based methods and markedly reduces computational cost compared to conventional fitting.

## KEYWORDS:

deep learning, computer-assisting image processing, magnetic resonance imaging, radiology

Chemical shift-encoded MRI (CSE-MRI) is a reliable, fast method for quantifying proton density fat fraction (PDFF) in a wide variety of organs and disease states<sup>1,2,3,4,5</sup>. PDFF measurements are now established for the measurement of steatosis in liver<sup>5</sup>, and are also increasingly used for other organs including pancreas<sup>6,7</sup>, muscle<sup>8</sup> and bone marrow<sup>9,10</sup>. CSE-MRI most commonly utilises multi-echo gradient-echo gradient echo acquisitions, meaning that  $R_2^*$  measurements can be extracted from the same acquisition, providing additional quantitative information on iron or calcium. CSE-MRI using gradient echo acquisitions is therefore a flexible way of interrogating a wide variety of pathological processes. The speed of these acquisitions means that they are also suitable for whole body MRI (WB-MRI), which is becoming an important tool for cancer staging<sup>11,12,13</sup>, amongst other applications such as the assessment of inflammatory arthritis<sup>14</sup>.

From a signal processing perspective, the central challenge of CSE-MRI is to disentangle or separate the signals arising from water and fat. This is challenging because the signal arising from water-dominant and fat-dominant tissues is very similar, giving rise to the so-called 'fat-water ambiguity' problem. The prevailing approach to solving this problem has been to use the phase of the complex signal in order to separate water and fat: with complex signal-based methods, water-dominant and fat-dominant tissues can be distinguished on the basis of their phase, so long as the contribution to the phase from main magnetic field  $B_0$  can be estimated accurately and therefore separated from the phase arising due to chemical shift<sup>1,2,3,4,5</sup>. Despite the progress that has been achieved by these complex-based methods<sup>1,2,3,4,5</sup>, fat-water swaps still occur and can mimic or hide important abnormalities<sup>15</sup>, meaning that avoiding such swaps remains a research focus, both for standard gradient echo CSE-MRI<sup>16</sup> and to enable the estimation of fat-corrected qMRI parameters<sup>17</sup>. Additionally, in emerging fields such as imaging near metal<sup>18</sup> and small bowel MRI<sup>19</sup>, fat suppression methods need to deal with large  $B_0$  variations, where existing fat suppression methods commonly fail. An alternative to complex signal-based methods is to discard the phase and use only the magnitude of the signal for parameter estimation: this has the advantage that the difficulty in estimating  $B_0$  is avoided, but the disadvantage that a further source of information is required to resolve fat-water ambiguity. It has recently been shown that the ambiguity between water-dominant and fat-dominant tissues can be resolved on the basis of subtle differences in the oscillations of the magnitude signal over multiple echoes, providing a mechanism to overcome this barrier<sup>20,21</sup>.

An additional challenge for CSE-MRI methods is computational cost. In the case of complex signal-based methods,

this cost can arise from the use of image-based optimisation methods such as iterative region-growing methods<sup>22,23</sup> or graph cut algorithms<sup>3,24,25,26</sup>, which aim to jointly estimate  $B_0$  in multiple voxels across the image, or from performing fitting within each voxel (so called 'voxel-independent' fitting), which is often performed as a subsequent step<sup>27,28</sup>. In the case of magnitude-based methods, the use of expensive image-based methods is typically avoided, but the computational cost is nonetheless increased by the need to perform fitting with nonlinear least squares several times (with different start points) in order to ensure that the correct likelihood maximum / error minimum is found<sup>20,21</sup>. The computational cost of fat-water separation poses a barrier to its use in research settings and in clinical practice.

As a result of these limitations, there has been interest in using deep learning to reduce the cost of fat-water separation and reduce artefacts. The use of deep learning for model fitting has the advantage that computational cost is front-loaded: model training can be performed in advance, before images are acquired, and the computational resources needed to actually process those images are typically much less than with conventional fitting.

So far, most authors have used convolutional neural networks to separate fat and water, exploiting the spatial relationships in the image as well as the information contained within individual voxels in the echo dimension<sup>29,30,31,32</sup>. However, a disadvantage of this CNN-based approach is that the network is trained on images from a specific anatomical region, and may not be generalizable to other regions of the body. CNN-based methods may also be vulnerable to differences in acquisition parameters such as image matrix. Furthermore, training networks using this approach is typically extremely slow, with training taking many hours or even days<sup>29,30,31,32</sup>.

An alternative approach, which may be more robust to variations in anatomy and acquisition parameters as well as several orders of magnitude faster, is to perform fat-water separation in a 'voxel-independent fashion', i.e. perform parameter estimation separately in each voxel. However, to date there are no studies addressing this issue. We suggest that this could be because (1) fat-water ambiguity cannot be reliably resolved in individual voxels using complex data (the field map) due to  $B_0$  inhomogeneity and (2) using magnitude data, whilst avoiding the problems with  $B_0$  inhomogeneity, creates a difficulty in fitting due to degeneracy: there are two potential sets of parameter values which produce very similar signals.

To address these issues, we propose RAIDER, a method for **rapid, anatomy-independent deep learning-based CSE-MRI**. With RAIDER, parameter estimation is performed separately in each voxel using deep learning. The method relies on paired multilayer perceptrons (MLPs) that are trained separately, each with a training distribution that is restricted in

order to avoid degeneracy, before choosing the optimal parameter estimates from the two networks based on the difference in likelihood.

## 2 | THEORY

### 2.1 | Tissue and noise models

A full description of the tissue and noise models used in this work is given in<sup>21</sup>; the key tissue and noise models are briefly summarised here.

With a gradient-echo based CSE-MRI acquisition, the noise-free complex signal  $S$  acquired at echo time  $t$  can be modelled as:

$$S(t|\rho_w, \rho_f, R_2^*, f_B) = \left( \rho_w + \rho_f \sum_{m=1}^M r_m e^{i2\pi f_{F,m} t} \right) e^{i2\pi f_B t} e^{-tR_2^*} \quad (1)$$

where  $\rho_w$  and  $\rho_f$  are the amplitudes of water and fat components,  $f_{F,m}$  is the frequency of each spectral fat component,  $r_m$  is the relative amplitude of each spectral fat component,  $M$  is the total number of spectral fat components,  $f_B$  is the frequency offset due to  $B_0$  inhomogeneity and  $R_2^* = 1/T_2^*$  is an unknown relaxation constant. It is conventional to assume that the relative amplitudes and frequency offsets of each fat component are known *a priori*; therefore the unknown parameters are  $\rho_w$ ,  $\rho_f$ ,  $f_B$  and  $R_2^*$ . Having determined  $\rho_w$  and  $\rho_f$ , the proton density fat fraction (PDFF) is calculated using  $\text{PDFF} = \rho_f / (\rho_f + \rho_w)$ .

In the presence of Gaussian noise (present in both real and imaginary channels), the log likelihood for a set of predicted signals, given the measured signals, is given by

$$\log L(\{S_i\}, \sigma^2 | \{S'_i\}) = -n \log(\sqrt{2\pi\sigma^2}) - \sum_{i=1}^n \frac{|S'_i - S_i|^2}{2\sigma^2} \quad (2)$$

where  $\{S_i\}$  is the set of predicted signals based on the parameter estimates,  $\{S'_i\}$  is the set of measured signals,  $\sigma^2$  is the variance of the Gaussian distribution for the noise,  $n$  is the number of measurements (double the number of echo times for complex data, or the number of echo times for magnitude data).

For the signal magnitude, the noise-free signal in Eqn (1) becomes

$$M(t|\rho_w, \rho_f, R_2^*) = \left| \rho_w + \rho_f \sum_{m=1}^M r_m e^{i2\pi f_{F,m} t} \right| e^{-tR_2^*} \quad (3)$$

with only three unknown parameters:  $\rho_w$ ,  $\rho_f$ , and  $R_2^*$ .

Taking the magnitude dictates that the noise now has a Rician distribution. The log likelihood for a set of predicted

signals becomes

$$\log L(\{M_i\}, \sigma^2 | \{M'_i\}) = \sum_{i=1}^n \left[ \log \frac{M'_i}{\sigma^2} - \frac{M_i'^2 + M_i^2}{2\sigma^2} + \log I_0\left(\frac{M'_i M_i}{2\sigma^2}\right) \right] \quad (4)$$

where  $\{M'_i\}$  is the set of measured magnitude signals at different echo times,  $\{M_i\}$  is the corresponding set of predicted magnitude signals and  $I_0$  is the 0<sup>th</sup> order modified Bessel function of the first kind.

### 2.2 | Dual optima problem and the source of degeneracy in CSE-MRI

With magnitude-based fitting, the likelihood functions defined in Eqns (2) and (4) have two optima: one 'true' solution corresponding closely to the ground truth and one incorrect 'swapped' solution with a PDFF value at the opposite end of the range (i.e. with a PDFF value close to 1 - PDFF) (Fig. 1). This creates a source of degeneracy - for a given set of signals, there are two candidate solutions which have very similar likelihood. The MAGO and MAGORINO methods used two-point search to ensure that both optima are explored<sup>20,21</sup>, and thus ensure that the global optimum would correspond to the true solution. However, this degeneracy can create a problem for deep learning, as outlined in Section (2.4).

Note that there is a stationary or 'switching' point (in 1D) or line (in 2D) close to 60% PDFF, below which the any initial guesses are likely to converge to the low PDFF solution and above which the initial guesses are likely to converge to the high PDFF solution. This is relevant to the degeneracy problem discussed in 2.4.

### 2.3 | Parameter estimation with deep learning

The use of deep learning for curve fitting was first proposed by Bishop<sup>33</sup>, and in recent years has become increasingly widely used for qMRI parameter estimation. As with conventional fitting, a model is fit to the acquired measurements. However, instead of finding the points on the objective function at which error is minimized / likelihood is maximised, a deep neural network is trained to directly map a single voxel's signal to its corresponding qMRI parameters<sup>33</sup>. The unknowns in this model are thus the network weights rather than the parameters in the signal model. Once the network has been trained, parameter estimation can simply be achieved by inputting unseen data to the network, one voxel at a time. This effectively front-loads the computational cost and means that the cost at the time the network is applied is dramatically reduced compared to conventional fitting.

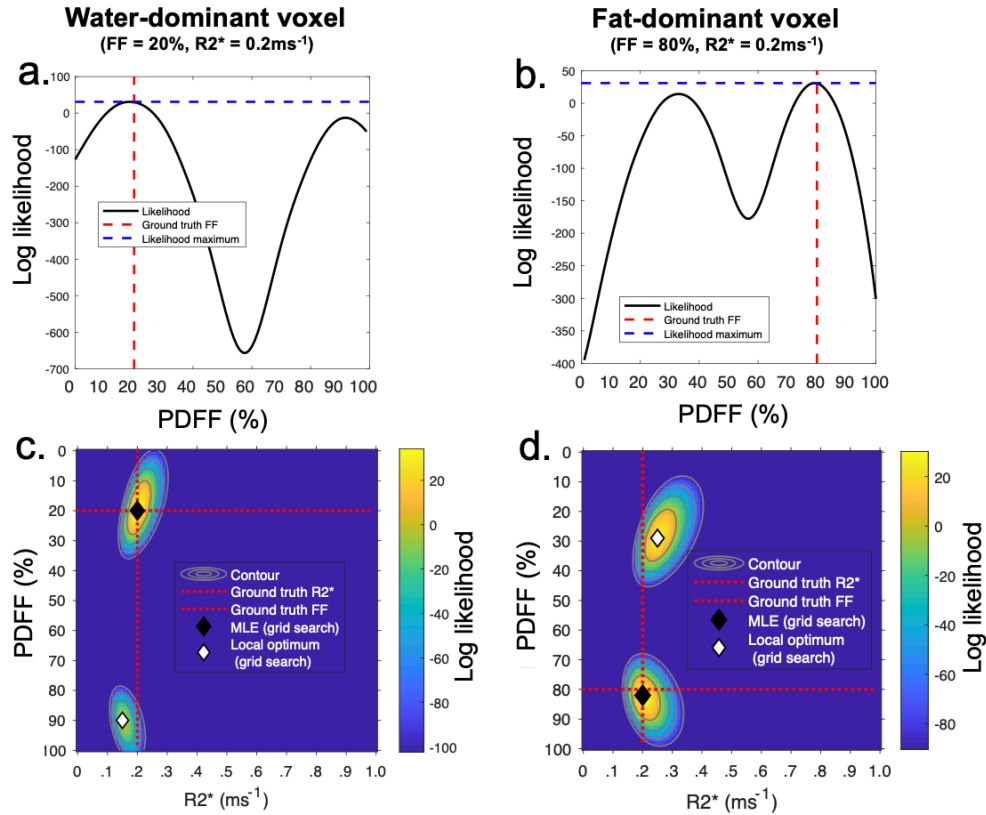


**FIGURE 1** Conceptual illustration of dual-optimum problem and how this leads to degeneracy. The Gaussian likelihood is shown as a function of PDFF for water-dominant voxels (PDFF=20%) (a,c) and fat-dominant voxels (PDFF=80%) (b,d). On the 1-D plots (a,b), ground truth estimates and the maximum/optimum likelihood are shown as red and blue dotted lines respectively. On the 2D plots (c,d), the ground truth is shown with red dotted crosshairs; the global and local likelihood optima are shown as black and white diamonds respectively. For both water-dominant and fat-dominant voxels, there are two optima occurring at low PDFF and high PDFF. This creates a source of degeneracy - for a given set of signals, there are two candidate solutions which have very similar likelihood.

## 2.4 | Degeneracy in deep learning

Bishop noted that neural networks were able to represent one-to-one and many-to-one mappings, but could not represent one-to-many ('multivalued') mappings<sup>33</sup>. This problem was referred to by Bishop as an 'ambiguity phenomenon' and is referred to here as degeneracy. In Bishop's experiments, the quality of the neural network fits was found to be very poor in regions of parameter space where this degeneracy problem occurred. Guerreri et al. recently provided further theoretical insights into this problem, showing that, in the presence of degenerate samples during training, the function learned by the neural network during training will map the degenerate signal to the empirical mean of tissue properties over the degenerate subset<sup>34</sup>. In other words, in this situation the network does not learn either of the correct solutions. This creates a particular problem for CSE-MRI, where there are two candidate solutions (the 'true' solution and the 'swapped' solution) with very similar likelihood.

Bishop suggested that, in cases where there were multiple potential solutions for a given input, this problem could be solved by excluding a region of the output space<sup>33</sup>. However, this approach assumes that one region of output space can be discarded on the basis that it is unlikely to occur in experiment. With CSE-MRI, this is not a satisfactory solution because both low PDFF and high PDFF values can be present in real tissue.

To address this, we propose dividing the parameter space into two parts, in such a way that one network can be trained on the first part of parameter space, and the other network can be trained on the second part of parameter space, without degeneracy. Specifically, we divide the parameter space into low PDFF regions, with PDFF values below the switching line, and high PDFF regions, with PDFF values above the switching line. In this way we create two networks that are each accurate within the region of parameter space on which they are trained. We propose that the correct output of the

two networks can then be chosen based on the difference in likelihood (as defined in Eqn (4)) between the two solutions.

### 3 | METHODS

#### 3.1 | Network

##### 3.1.1 | Network architecture

A simple network design consisting of five fully-connected hidden layers, each with the same number of nodes as the number of signal measurements (i.e. echo times), and an output layer with a node for each model parameter, with exponential linear unit (ELU) activation functions, was used. The network was trained in a supervised fashion using parameter values (labels) randomly drawn from PDFFF /  $R_2^*$  parameter space and the corresponding simulated noise-free signal intensities (features). The network was implemented in Matlab 2021b on an Apple iMac with 3.8-GHz 8-Core Intel i7 processor using the central processing unit (CPU).

##### 3.1.2 | Network training

The network was trained using an Adam optimiser with learning rate 0.001, minibatch size 32, validation patience 20, maximum number of epochs 1000, and L2 regularisation 0. All processing was performed in MATLAB 2021b (MathWorks, Natick, MA). Further details of network training are detailed in the individual experiments below.

##### 3.1.3 | Normalisation

To make the network predictions robust to variations in signal intensity (i.e. variations in  $S_0 = \rho_w + \rho_w$ ), the multiecho signals were normalised by an approximation of  $S_0$ . This approximation was obtained by taking the measured signal for the two echo times closest to the first and second in phase echo times, calculating the decay between these echo times (assuming monoexponential decay) and then extrapolating back to  $t = 0$ . For simulation experiments, this step is not strictly necessary because  $S_0$  is specified and therefore known *a priori*, however, we included this normalisation step in these experiments (as well as for the real data) to ensure that the results were as fair a representation as possible of the situation expected *in vivo*, where  $S_0$  is unknown.

Note that a slightly different normalisation procedure to the above was used at the stage of deciding which of the two network outputs to select: for this step an image-based normalisation, whereby the signal intensity in each voxel was divided by the maximum intensity in the image, was used. Using this

alternative normalisation at the output selection stage provided the correct selection of the output in a higher proportion of voxels than the normalisation above.

#### 3.2 | Simulation Experiments

A series of simulation experiments were conducted to investigate the effect of training data distribution on the accuracy and precision of parameter estimation. For all of the experiments, the training data was constructed from multi-echo signals simulated using Equation (3) for a range of PDFFF and  $R_2^*$  values using a typical CSE-MRI acquisition protocol with ten echotimes, with  $TE_1 = 1.1$  ms and  $\Delta TE = 1.1$  ms.

The distribution of PDFFF and  $R_2^*$  values was varied for each experiment by defining regions of parameter space from which the PDFFF and  $R_2^*$  values could be selected, as detailed below and in Figure 2. PDFFF and  $R_2^*$  values were randomly selected within the defined region.

Performance was evaluated on a separate simulated test dataset consisting of evenly-spaced PDFFF and  $R_2^*$  values across the full parameter space (PDFFF  $\in [0, 1]$ ,  $R_2^* \in [0, 500]$  s<sup>-1</sup>).

##### 3.2.1 | Single network with uniform training distribution; testing with noise-free data

The training dataset consisted of 20,000 signals generated with a uniform distribution in PDFFF /  $R_2^*$  parameter space (PDFFF  $\in [0, 1]$ ,  $R_2^* \in [0, 500]$  s<sup>-1</sup>), as demonstrated in Figure 2 (a).

##### 3.2.2 | Dual networks with modified training distribution; testing with noise-free data

To address the effect of degeneracy on network predictions, two training datasets, each consisting of 20,000 signals, were constructed from the following parameter distributions (as demonstrated in Figure 2 (b,c)):

The first network ('water network') was trained only on the low PDFFF dataset, i.e. with PDFFF values below the switching line (PDFFF  $\in [0, 0.63]$ ,  $R_2^* \in [0, 500]$  s<sup>-1</sup>).

The second network ('fat network') was trained only on the high PDFFF dataset, i.e. with PDFFF values above the switching line (PDFFF  $\in [0.63, 1]$ ,  $R_2^* \in [0, 500]$  s<sup>-1</sup>).

Having trained these two networks and obtained the predictions on the test dataset, a further set of 'composite' predictions was derived by choosing the output from the two networks with the highest likelihood based on Eqn (4), as demonstrated in Figure 2. Additionally, where physically implausible parameter estimates were generated by one network (specifically, where  $R_2^*$  estimates were less than zero), which typically occurred when the fat network was making

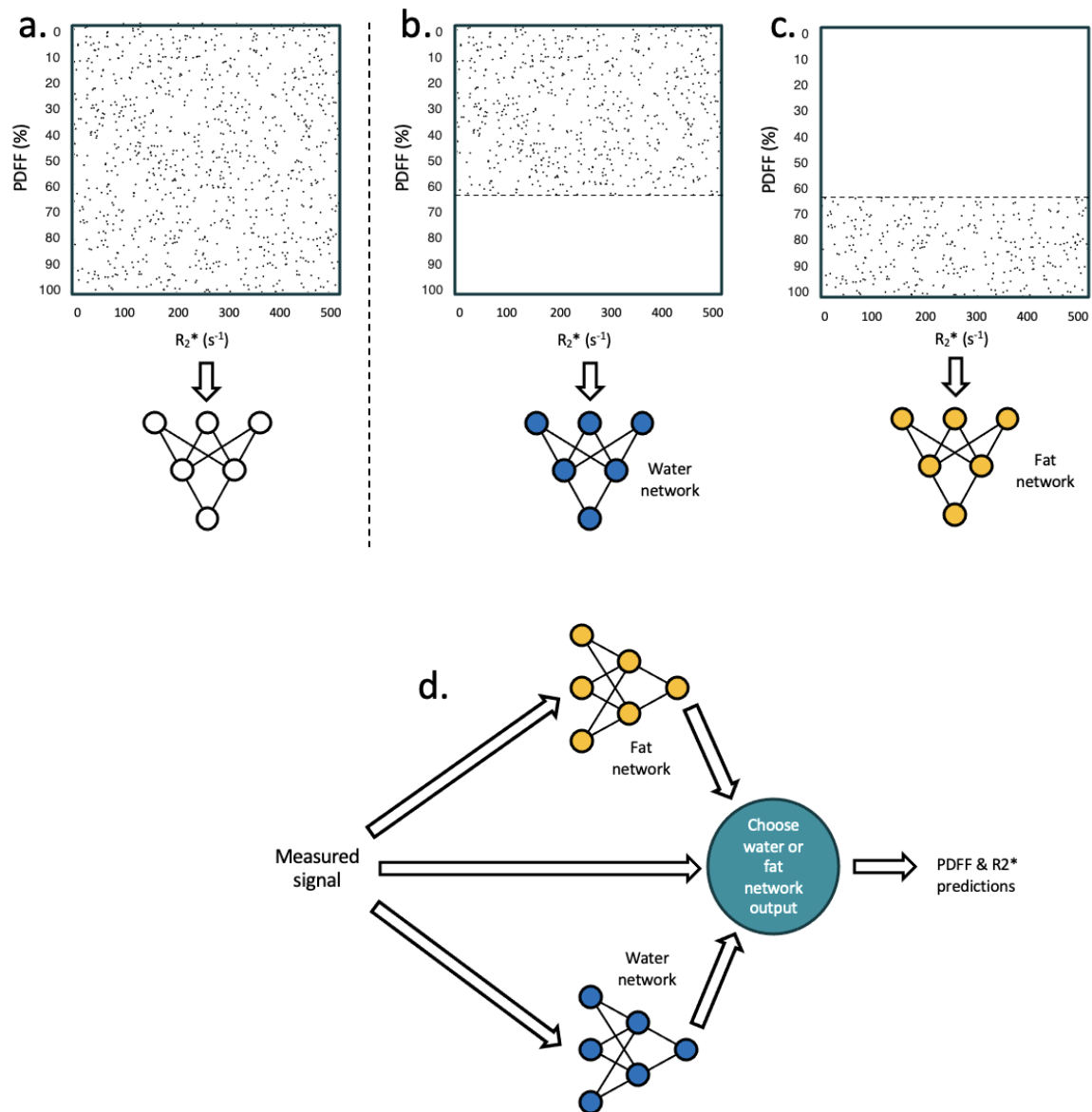


**FIGURE 2** Training procedure for single and dual network approaches. With the conventional approach (a), a single network is trained with a uniform distribution across the full training range. With the proposed approach, two separate networks are trained on separate parts of parameter space to avoid degeneracy: a 'water network' (b) is trained only on the region of parameter space below the 'switching line' (dashed line), and a 'fat network' (c) is trained only on the region of parameter space above the switching line (dashed line). The outputs from the two networks (fat network and water network) are treated as 'candidate' solutions; the likelihood for each candidate is calculated based on the measured signal and the one with the higher likelihood is selected (d).

predictions in the regions of parameter space on which it had not been trained, it was assumed that the other network was the correct choice.

### 3.2.3 | Dual networks with modified training distribution; testing with noisy data

To investigate performance in the presence of noise, the test dataset used for the experiments in Sections 3.2.1 and 3.2.2 was extended such that 100 noisy signals (at SNR = 60, which

is typical for CSE-MRI) were generated for each PDFF /  $R_2^*$  combination (101 x 21 x 100 = 212100 instantiations in total across all parameter values). The performance of the composite predictions (i.e. the chosen output of the two networks) from the two networks trained in Sections 3.2.1 and 3.2.2 was evaluated in terms of accuracy and precision over these 100 noisy signals, and compared against conventional fitting. Conventional fitting was implemented using the MAGORINO algorithm<sup>21</sup>, and also with an in-house implementation of the MAGO algorithm<sup>20</sup>.

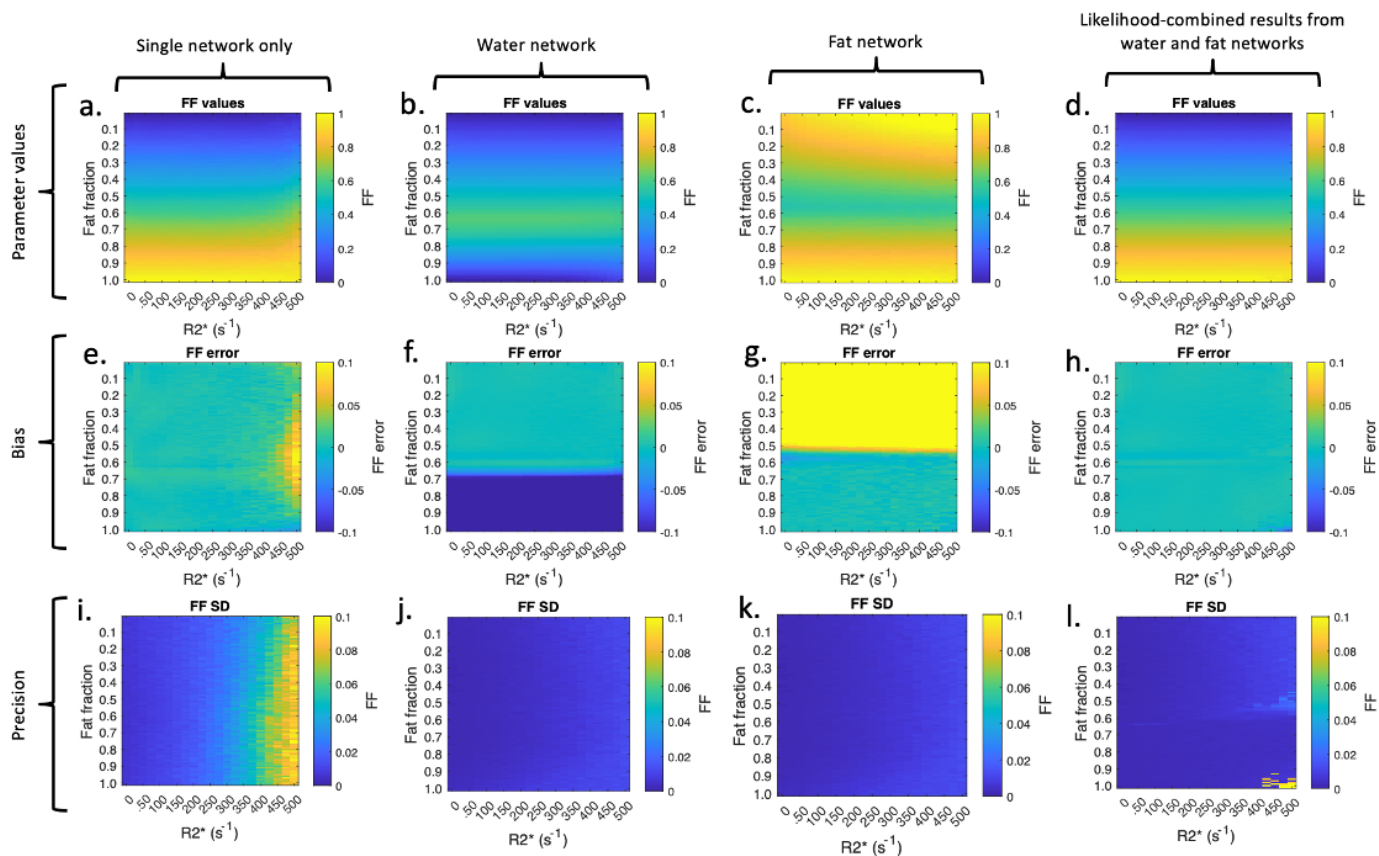


**FIGURE 3** Improvement in performance for dual network approach compared to single network. The figure shows the performance of a single network with no restriction of training distribution (left column), individual water and fat networks (second and third columns) and likelihood-combined networks (right column). The parameter values are shown on the top row, bias is displayed in the middle row and parameter standard deviation is shown on the bottom row.

### 3.3 | Phantom experiments

To evaluate the feasibility of DL-based fitting across a range of scanners, our method was evaluated in a publicly available multisite, multivendor, and multi-field-strength phantom data set<sup>28</sup>. The dataset consists of fat–water mixtures with known varying fat fraction, scanned at 1.5 T and 3 T at six centers (two centers each for GE, Philips, and Siemens). Data acquisition was performed using each site’s version of a multi-echo 3D spoiled gradient-echo CSE sequence, with two different protocols (each performed at 1.5T and 3T) used to test the reproducibility across different acquisition parameters. Protocols 1 and 2 were performed at 1.5 T, and protocols 2 and 4 were performed at 3 T. Protocols 1 and 3 generated approximately in-phase and opposed-phased echoes, whereas protocols 2 and 4 used the shortest echoes achievable.

Deep learning-based parameter estimation was performed as described in Sections 3.2.2 and 3.2.3. After generating parameter maps, fat fraction values were obtained from the individual vials of the phantom by taking the median value from ROIs placed on the individual tubes, and were compared against known reference values using linear regression. The

performance of the networks was compared against conventional fitting.

### 3.4 | In vivo imaging

To evaluate the feasibility of the proposed approach *in vivo*, we imaged the pelvis, lower legs and thorax/abdomen of three separate subjects. The pelvis and lower leg data were acquired on a 3T Philips Ingenia system using a multi-echo 3D spoiled gradient-echo sequence with flyback gradients and monopolar readouts  $TE_1 = 1.2$  ms,  $\Delta TE = 1.6$  ms, flip angle =  $5^\circ$ ,  $TR = 25$  ms, matrix size =  $320 \times 320$ , and pixel spacing =  $1.8 \times 1.8$  mm. The thoraco-abdominal imaging was performed on a Siemens 3T Vida scanner using a similar acquisition with  $TE_1 = 1.1$  ms,  $\Delta TE = 1.1$  ms; for these acquisitions the Siemens qDixon package was used to generate vendor-supplied PDFF maps, providing a further reference standard. Deep learning-based parameter estimation was performed as described in Sections 3.2.2 and 3.2.3. These scans were performed with institutional review board approval (Queen Square Research

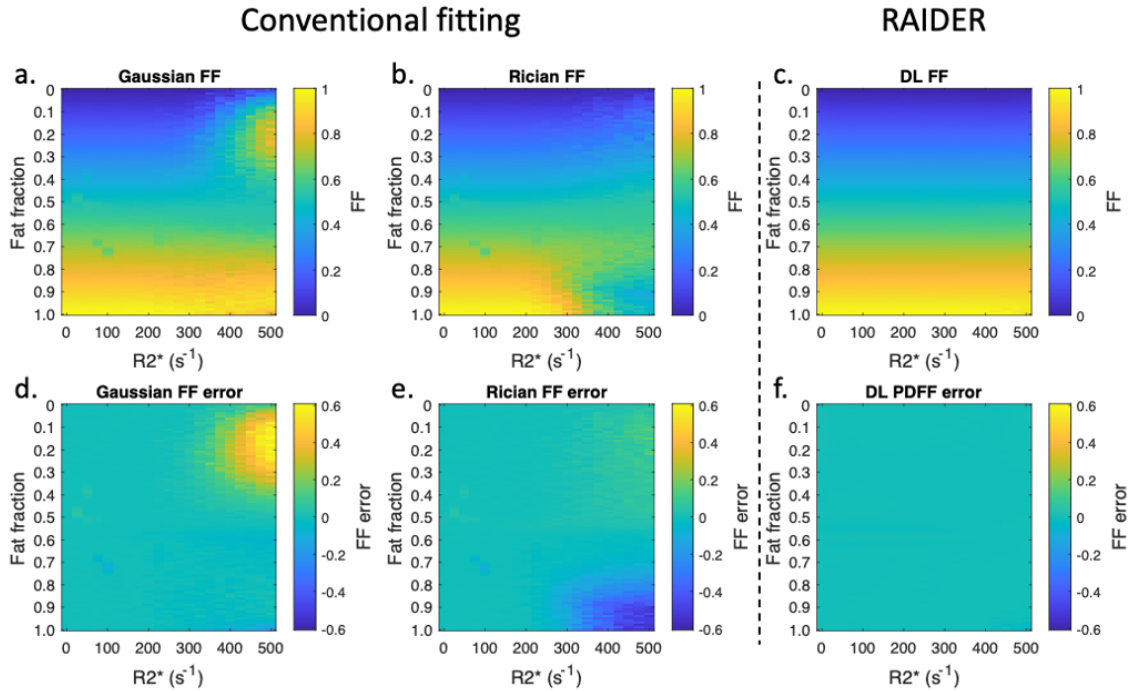


**FIGURE 4** Performance of chosen output from two networks in the presence of noise and comparison against conventional fitting.

Ethics Committee, London, REC 15/LO/1475), and subjects provided written informed consent.

## 4 | RESULTS

### 4.1 | Simulation experiments

#### 4.1.1 | Uniform training distribution; noise-free evaluation

Figure 3 (left column) shows the performance of a single network trained with a uniform distribution of parameter values over the full parameter space. There are regions of positive error (shown in yellow) towards the right of subplot (e) (i.e. with increasing  $R_2^*$ ); whilst the precision of parameter estimates (i) deteriorates substantially with increasing  $R_2^*$ .

#### 4.1.2 | Modified training distribution with dual networks; noise-free evaluation

The second column of Figure 3 shows the performance of a single network trained with a restricted, low PDFFF distribution of parameter values (the 'water network'). Compared to the single network, there is a substantial improvement in performance for low PDFFF values, with elimination of the high error, high variance regions at high  $R_2^*$ . However, as expected, the network fails on the high PDFFF values as it as not experienced this region of parameter space during training.

Similarly, the third column of Figure 3 shows the performance of a single network trained with a restricted, high PDFFF distribution of parameter values (the 'fat network'). Compared to the single network, there is a substantial improvement in performance for high PDFFF values, particularly at high  $R_2^*$ . As expected, the network fails on the low PDFFF values as it as not experienced this region of parameter space during training.

The right-hand column of Figure 3 shows the 'combined' performance of the two networks (i.e. the performance of the chosen output of the two networks based on likelihood). Compared to the single network (left column), the performance is substantially improved, both in terms of bias and precision. There is a tiny region of poor precision in the bottom right corner of (l), indicating that the incorrect solution is chosen in some cases in this region of parameter space.

#### 4.1.3 | Modified training distribution with dual networks; evaluation in the presence of noise

Figure 4 shows the combined performance of the two networks in the presence of noise, compared against conventional fitting. The overall performance is superior to conventional fitting using both Gaussian and Rician likelihood models, with minimal error for all fat fraction and  $R_2^*$  values, whereas the conventional fitting methods both show deteriorating performance as  $R_2^*$  increases.



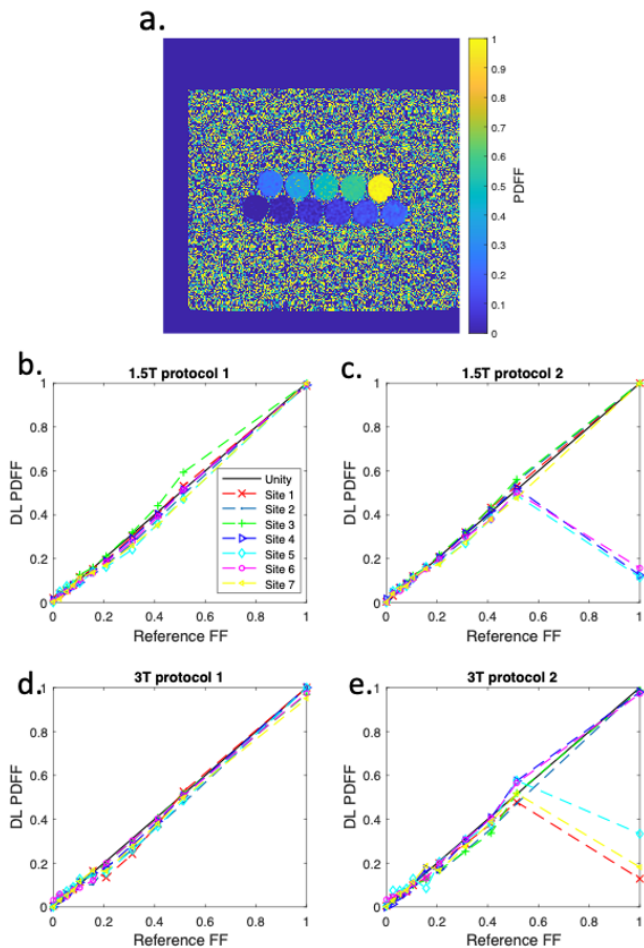


**FIGURE 5** Results from multisite, multivendor, multi-field-strength phantom data set. Agreement plots are shown for each of the four protocols, with individual points for each of the six sites. The black line indicates perfect agreement with reference PDFF values. “Site 7” refers to the repeat scans at site 1. The example image (top) is from site 1, 3T protocol 2, chosen to enable a direct visual comparison with corresponding illustrations in the MAGO and MAGORINO papers<sup>20,21</sup>.

## 4.2 | Phantom experiments

Results of the analysis of the multisite phantom data set are shown in Figure 5.

Median PDFF values for all 11 phantom vials are plotted against reference fat fraction values for all sites, acquisition protocols, and field strengths. Linear regression results are found in Supporting Information (slope, intercept, and R-squared). There is good agreement between the predictions and the reference values with high accuracy, high linearity, and small bias (reflected in R-squared coefficients close to 1, slope close to 1, and intercept close to 0) across vendors and field strengths for protocol 1. For protocol 2, there were some cases of failure at the pure fat vials, indicating a degree of protocol dependence at the network output selection step (similar to with conventional MAGORINO fitting)<sup>21</sup>.

## 4.3 | In vivo imaging

Images from the three subjects are shown in Figures 6, 7 and 8. In all subjects, the composite predictions produced satisfactory fat–water separation across the image and good-quality  $R_2^*$  maps. Figure 6 shows that there is a small bias in the subcutaneous fat for RAIDER compared to the conventional fitting. Figure 7 shows good agreement between RAIDER and conventional fitting, with slightly superior fat–water separation in the subcutaneous fat for RAIDER. Figure 8 shows that RAIDER also agrees closely with vendor-produced PDFF maps, providing a further, separate corroboration of the performance of the method.

## 4.4 | Fitting speed

RAIDER was approximately 700 times faster than conventional fitting, taking 14  $\mu s$  per voxel, compared to 10 ms for conventional fitting with MAGORINO<sup>21</sup>. This equates to 1.3s vs 15 minutes for a 300x300 slice).

## 5 | DISCUSSION

There has been substantial recent interest in the use of deep learning-based methods for CSE-MRI to improve the quality of fat–water separation and reduce computational cost. However, previous attempts have relied on the use of convolutional neural networks (CNNs), which have limitations in terms of training data requirements, generalizability and speed (with training taking many hours or even days)<sup>29,30,31,32</sup>. Using deep learning to separate water and fat in a ‘voxel-independent fashion’, performing parameter estimation separately in each voxel, is likely to be more generalizable as well as much faster than CNN-based approaches, since it does not require real data for training and can be easily trained for any protocol, using only simulated data. However, to our knowledge no previous studies have addressed this issue, possibly because of the degeneracy problems discussed in this manuscript. Here, we propose an approach to resolving this degeneracy issue, using two neural networks trained separately with restricted training distributions. By resolving the degeneracy problem, our method address the limitations of CNN-based methods and also offers a substantial reduction in computational cost compared to conventional fitting.

The key results of our study are as follows. Firstly, we found that using a single network with a full training distribution, including all plausible PDFF and  $R_2^*$  values, produces relatively poor performance, with substantial imprecision at high  $R_2^*$ . Secondly, we showed that performance could be improved by training individual networks on a restricted distribution of parameter values: specifically, by training one network only on low PDFF values (below the switching line) and

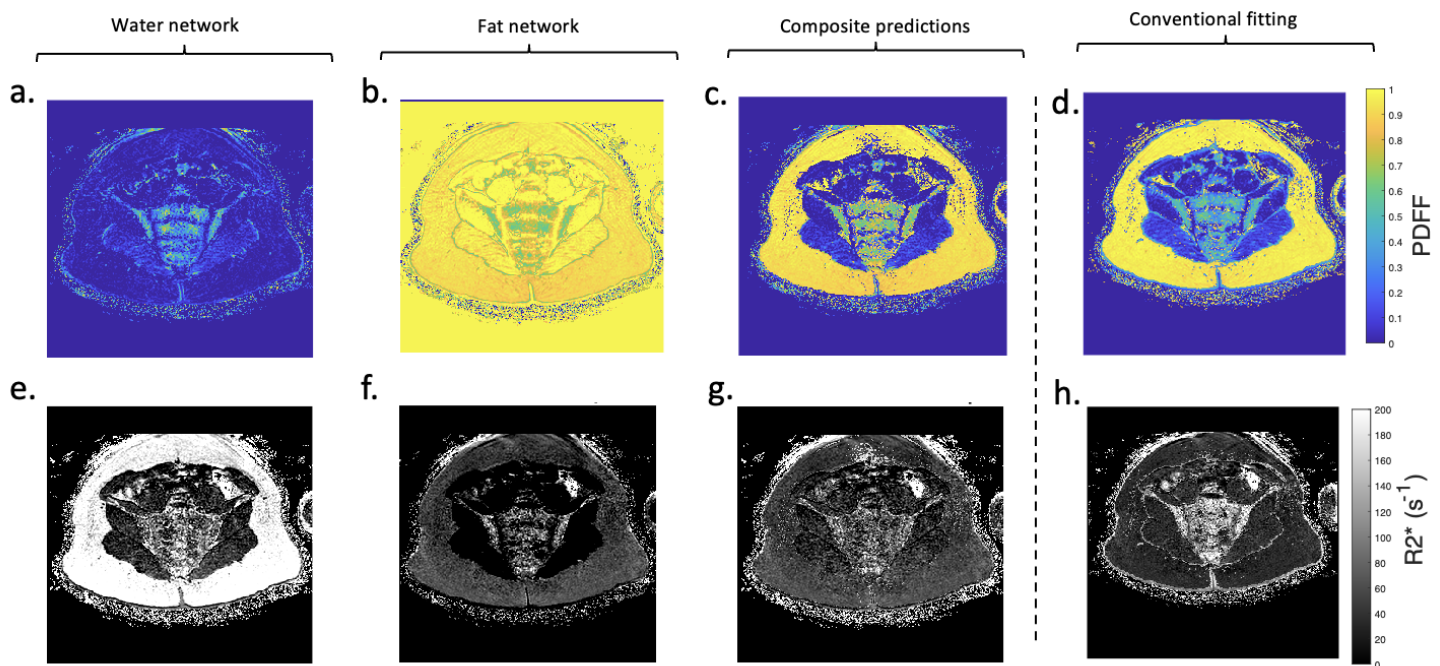


**FIGURE 6** PDFF maps (top row) and  $R_2^*$  maps (bottom row) from the pelvis of a volunteer. Note that the water network (left column) produces exclusively low PDFF estimates whereas the fat network (middle column) produces exclusively high PDFF estimates. However, the chosen output from the two networks based on likelihood (right column) produces plausible predictions across a range of tissue types, including adipose tissue (almost pure fat), muscle (almost pure water) and bone marrow (approximately equal fat and water content). The composite predictions agree closely with these obtained with conventional fitting, although there is a small negative bias in the adipose tissue for RAIDER.

another on high PDFF values (above the switching line). By selecting the most likely result from these networks, we were able to obtain predictions that substantially outperformed the naive case across the full parameter space. Thirdly, this deep learning-based method outperformed conventional fitting in terms of bias, precision and speed, with an approximately 700 fold acceleration. Finally, we showed that this method could be successfully implemented with real data. These results suggest that the proposed method could help to reduce the time and expense associated with processing of CSE-MRI data for research and in clinical practice, as well as potentially improving performance compared to conventional fitting.

Notably, there is a parallel between the approach used in this work, where two networks are used to separately obtain low PDFF and high PDFF solutions, with the conventional fitting-based MAGO and MAGORINO methods, where fitting is initiated twice from two different start points in order to ensure that the global optimum on the likelihood function is found<sup>20,21</sup>. Furthermore, the use of magnitude data retains the benefit of being essentially insensitive to  $B_0$  inhomogeneity, meaning that it could help to reduce artefacts at the edges of the field and in challenging situations such as when near metal, when imaging large subjects or when imaging anatomically complex structures, such as the small bowel.

This work has some limitations. Firstly, this is a 'proof-of-concept' study, and the evaluation with real data is preliminary. Secondly, in its present form the method does not account for Rician noise, which may create bias at low SNR, for example at low field strength. A practical solution to this would be to use a hybrid method whereby an initial fitting estimate is obtained using deep learning and then this initial estimate is refined using conventional fitting; this 'multi-step' approach has a clear precedent in the CSE-MRI literature<sup>28</sup>. Alternatively, Rician noise could be addressed through alternative DL approaches such as self-supervised learning<sup>35</sup>, which would avoid the cost associated with conventional fitting. Thirdly, the current method for choosing the correct output of the two networks (based on likelihood) is relatively simple and it is possible that a more sophisticated solution could be found, perhaps by using a third network to make this decision (this could have the advantage that different choices could be made in different regions of parameter space). Fourthly, the current implementation is entirely 'voxel-independent' (i.e. it only uses data from one voxel at a time), and it might be beneficial to incorporate additional, spatial information into the method. This could potentially be achieved by using small image patches (rather than individual voxels) as input to the network (which in this case might be a small CNN rather than an MLP).

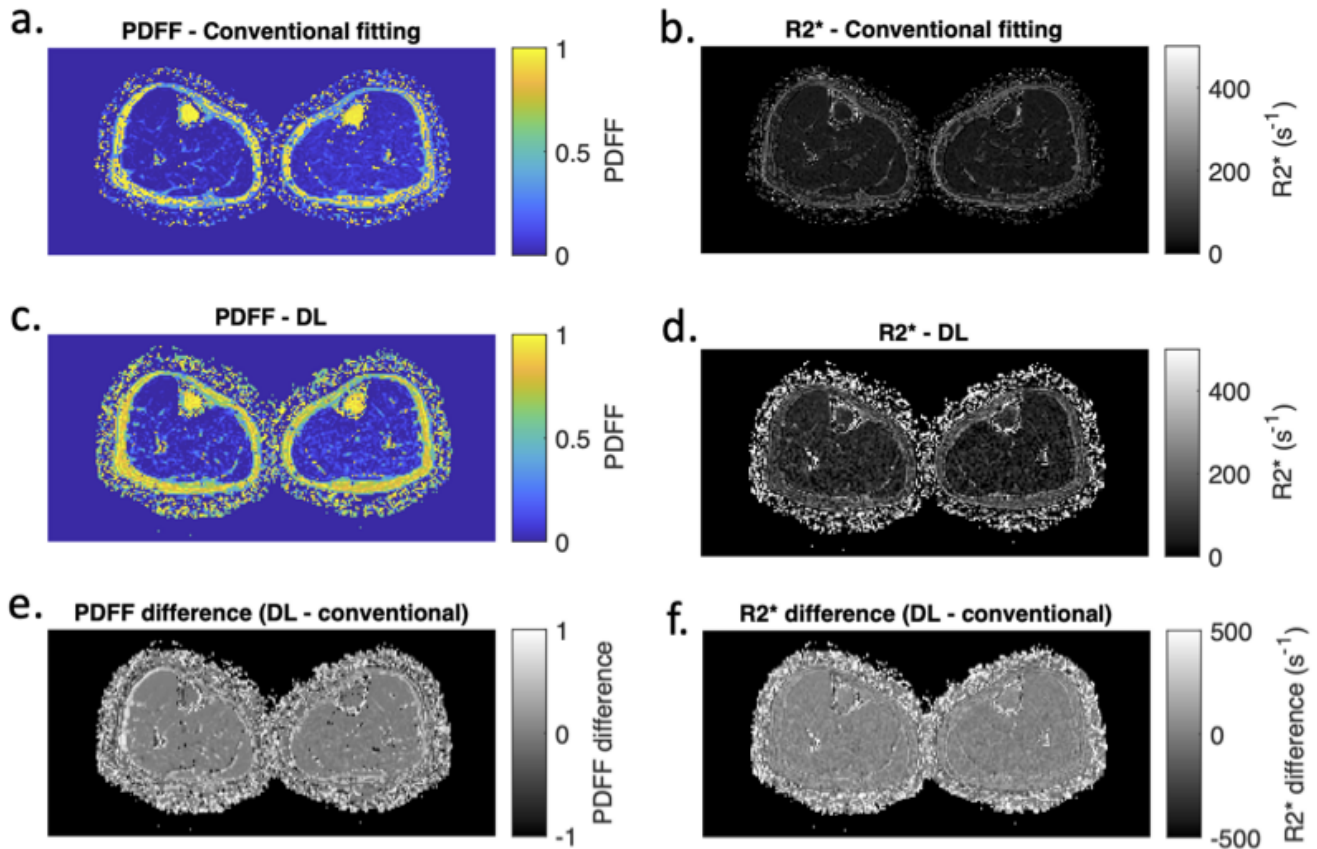


**FIGURE 7** Images of the lower legs in a volunteer. PDFFF maps (left column) and  $R_2^*$  maps (right column) are shown: the top row contains maps produced with conventional fitting, the middle row shows the deep learning-produced maps, and the bottom row shows difference maps.

## 6 | CONCLUSIONS

The paired neural network approach employed by RAIDER resolves the problems posed by degeneracy, avoids the training limitations of CNN-based methods and substantially reduces computational cost compared to conventional fitting.

### Financial disclosure

TJPB and MHC were supported by the UCLH National Institute for Health Research Biomedical Research Centre. This work was undertaken at UCLH/UCL, which receives funding from the UK Department of Health's NIHR BRC funding scheme. The funders had no role in study design, data collection and analysis, decision to publish, or preparation of the manuscript.

### Conflict of interest

The authors declare no potential conflict of interests.

### ORCID

Timothy JP Bray [ORCID](#) 0000-0001-8886-5356  
 Giulio V Minore [ORCID](#) 0009-0001-4529-8547  
 Alan Bainbridge [ORCID](#) 0000-0003-4941-5840  
 Stuart A Taylor [ORCID](#) 0000-0002-6765-8806  
 Margaret A Hall-Craggs [ORCID](#) 0000-0003-4941-5840  
 Hui Zhang [ORCID](#) 0000-0002-5426-2140

### REFERENCES

1. SB Reeder, Z Wen, H Yu, AR Pineda, GE Gold, M Markl, and NJ Pelc. Multicoil dixon chemical species separation with an iterative least-squares estimation method. *Magn Reson Med*, 51(1): 35–45, 2004.
2. SB Reeder, AR Pineda, Z Wen, A Shimakawa, H Yu, JH Brittain, GE Gold, CH Beaulieu, and NJ Pelc. Iterative decomposition of water and fat with echo asymmetry and least-squares estimation (ideal): Application with fast spin-echo imaging. *Magn Reson Med*, 54(3):636–644, 2005.
3. D Hernando, JP Haldar, J Ma, P Kellman, and Z-P Liang. Joint estimation of water/fat images and field inhomogeneity map. *Magn*

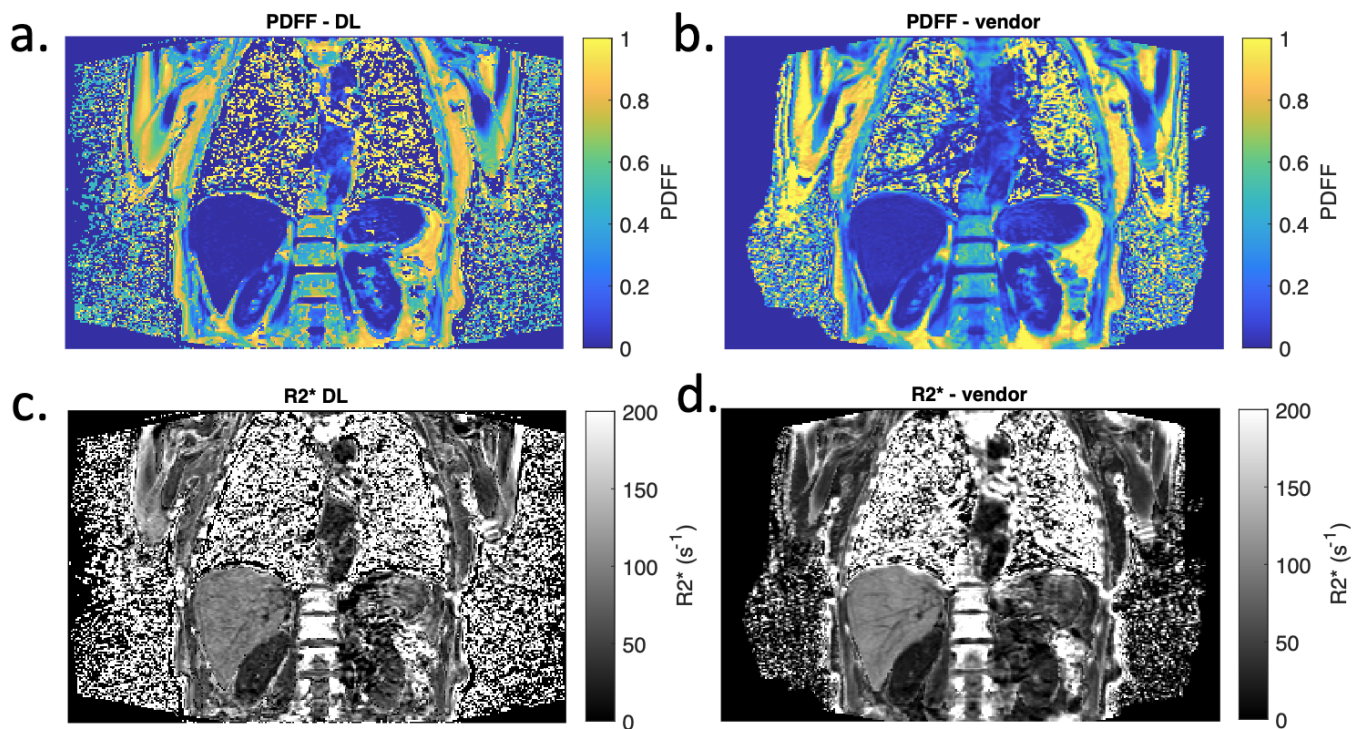


**FIGURE 8** Deep learning and vendor-reconstructed images of the the thorax and upper abdomen. PDFFF maps (top row) and  $R_2^*$  maps (bottom) are shown: the left column contains maps produced with deep learning, the right column shows the vendor-generated maps.

- Reson Med*, 59(3):571–80, 2008.
- CY Liu, CA McKenzie, H Yu, JH Brittain, and SB Reeder. Fat quantification with ideal gradient echo imaging: Correction of bias from t1 and noise. *Magn Reson Med*, 58(2):354–64, 2007.
  - M Nouredin, J Lam, MR Petereson, M Middleton, J Hamilton, Le T-A, R Betterncourt, C Changchien, DA Brenner, C Sirlin, and R Loomba. Utility of magnetic resonance imaging versus histology for quantifying changes in liver fat in nonalcoholic fatty liver disease trials. *Magn Reson Med*, 58(6):1930–1940, 2013.
  - JH Yoon, JM Lee, KB Lee, SW Kim, MJ Kang, JY Jang, S Kanngiesser, JK Han, and BI Choi. Pancreatic steatosis and fibrosis: quantitative assessment with preoperative multiparametric mr imaging. *Radiology*, 279:140–150, 2016.
  - JP Kuhn, F Berthold, J Mayerle, H Volzke, SB Reeder, W Rathman, MM Lerch, N Hosten, K Hegenscheid, and PJ Meffert. Pancreatic steatosis demonstrated at mr imaging in the general population: clinical relevance. *Radiology*, 276(1):129–136, 2015.
  - JM Morrow, CDJ Sinclair, A Fischmann, P Machado, MM Reilly, TA Yousry, JS Thornton, and MG Hanna. Mri biomarker assessment of neuromuscular disease progression: a prospective observational cohort study. *Lancet Neurol*, 15(1):65–77, 2016.
  - TJP Bray, A Bainbridge, S Punwani, Y Ioannou, and MA Hall-Craggs. Simultaneous quantification of bone edema/adiposity and structure in inflamed bone using chemical shift-encoded mri in spondyloarthritis. *Magn Reson Med*, 79(2):1031–1042, 2018.
  - A Latifoltojar, Hall-Craggs MA, A Bainbridge, N Rabin, R Popat, A Rismani, S D'Sa, N Dikaouis, M Sokolsa, M Antonelli, S Ourselin, K Yong, SA Taylor, S Halligan, and S. Punwani. Whole-body mri quantitative biomarkers are associated significantly with treatment response in patients with newly diagnosed symptomatic multiple myeloma following bortezomib induction. *Eur Radiol*, 27(12):5325–5336, 2017.
  - SA Taylor, SM Mallett, S Ball, S Beare, G Bhatnagar, A Bhowmik, P Boavida, and J. Bridgewater. Diagnostic accuracy of whole-body mri versus standard imaging pathways for metastatic disease in newly diagnosed non-small-cell lung cancer: the prospective streamline l trial. *Lancet Resp*, 7(6):523–532, 2019.
  - SA Taylor, SM Mallett, S Beare, G Bhatnagar, D Blunt, P Boavida, and J. Bridgewater. Diagnostic accuracy of whole-body mri versus standard imaging pathways for metastatic disease in newly diagnosed colorectal cancer: the prospective streamline c trial. *Lancet Gastro Hep*, 4(7):529–537, 2019.
  - CM Costelloe, V Kundra, J Ma, BA Chasen, EM Rohren, RL Bassett, and JE Madewell. Fast dixon whole-body mri for detecting distant cancer metastasis: a preliminary clinical study. *J Magn Reson Imaging*, 35(2):399–408, 2012.
  - V Choida, A-V Madenidou, D Sen, MA Hall-Craggs, and C Ciurtin. The role of whole-body mri in musculoskeletal inflammation detection and treatment response evaluation in inflammatory arthritis across age: A systematic review. *J Magn Reson Imaging*, 52:151953, 2022.
  - T Kirchgessner, S Acid, V Perlepe, F Lecouvet, and B Vande Berg. Two-point dixon fat-water swapping artifact: lesion mimicker at musculoskeletal t2-weighted mri. *Skeletal Radiology*, 49:2081–2086, 2020.
  - N Bastay, M Thanaj, M Cule, EP Sorokin, Y Liu, EL Thomas, JD Bell, and BW Whitcher. Artifact-free fat-water separation in dixon mri using deep learning. *J Big Data*, 10:4, 2023.
  - A Triay Bagur, D McClymont, C Hutton, A Borghetto, ML Gyngell, P Alijabar, MD Robson, M Brady, and DP Bulte. Estimation of field

inhomogeneity map following magnitude-based ambiguity-resolved water-fat separation. *Magn Reson Imag*, 97:102–111, 2023.

18. I Khodarahmi, A Isaac, EK Fishman, D Dalili, and J Fritz. Metal about the hip and artifact reduction techniques: from basic concepts to advanced imaging. *Sem Musc Radiol*, 23(3):e68–81, 2019.
19. D Boone and SA Taylor. Magnetic resonance of the small bowel: how to do it. 2020.
20. A Triay Bagur, C Hutton, B Irving, ML Gyngell, MD Robson, and M Brady. Magnitude-intrinsic water–fat ambiguity can be resolved with multipeak fat modeling and a multipoint search method. *Magn Reson Med*, 82(1):460–475, 2018.
21. TJP Bray, A Bainbridge, MA Hall-Craggs, and H Zhang. Magorino: Magnitude-only fat fraction and  $r2^*$  estimation with rician noise modelling. *Magn Reson Med*, 89:1173–1192, 2022.
22. H Yu, SB Reeder, A Shimakawa, JH Brittain, and NJ Pelc. Field map estimation with a region growing scheme for iterative 3-point water-fat decomposition. *Magn Reson Med*, 54:1032–1039, 2005.
23. J Berglund, L Johanson, G Ahlstrom, and J Kullberg. Three-point dixon method enables whole-body water and fat imaging of obese subjects. *Magn Reson Med*, 63:1659–1668, 2010.
24. C Cui, Xiaodong Wu, J Newell, and M Jacob. Fat water decomposition using globally optimal surface estimation (goose) algorithm. *Magn Reson Med*, 73:1289–1299, 2014.
25. C Cui, A Shah, Xiaodong Wu, and M Jacob. A rapid 3d fat–water decomposition method using globally optimal surface estimation (r-goose). *Magn Reson Med*, 79:2401–2407, 2017.
26. M Berglund and M Skorpil. Multi-scale graph-cut algorithm for efficient water-fat separation. *Magn Reson Med*, 78:941–949, 2016.
27. H Yu, A Shimakawa, CD Hines, CA McKenzie, G Hamilton, CB Sirin, JH Brittain, and SB Reeder. Combination of complex-based and magnitude-based multiecho water-fat separation for accurate quantification of fat-fraction. *Magn Reson Med*, 66:199–206, 2011.
28. D Hernando, SD Sharma, MA Ghasabeh, BD Alvis, SS Arora, G Hamilton, L Pan, and JM Shaffer. Multisite, multivendor validation of the accuracy and reproducibility of proton-density fat-fraction quantification at 1.5t and 3t using a fat–water phantom. *Magn Reson Med*, 77:1516–1524, 2017.
29. JW Goldfarb, J Craft, and JJ Cao. Water–fat separation and parameter mapping in cardiac mri via deep learning with a convolutional neural network. *J Magn Reson Imag*, 50:655–665, 2019.
30. J Andersson, H Ahlström, and J Kullberg. Separation of water and fat signal in whole-body gradient echo scans using convolutional neural networks. *Magn Reson Med*, 82:1177–1186, 2019.
31. R Jafari, P Spincemaille, J Zhang, TD Nguyen, X Luo, J Cho, D Margolis, MR Prince, and Y Wang. Deep neural network for water/fat separation: Supervised training, unsupervised training, and no training. *Magn Reson Med*, 85:2253–2277, 2021.
32. K Liu, Xiaojun Li, Y Chen, H Xiong, F Chen, Qinjia Bao, and C Liu. Robust water–fat separation based on deep learning model exploring multi-echo nature of mgre. *Magn Reson Med*, 85:2828–2841, 2021.
33. CM Bishop and CM Roach. Fast curve fitting using neural networks. *Rev Sci Instrum*, 63(10):4450–4456, 1992.
34. M Guerrerri, S Epstein, H Azadbakht, and H Zhang. Resolving quantitative mri model degeneracy with machine learning via training data distribution design. *Inf Process Med Imaging*, 2023.
35. S Epstein, TJP Bray, MA Hall-Craggs, and H Zhang. Choice of training label matters: how to best use deep learning for quantitative mri parameter estimation. *arXiv*, page 2205.05587, 2022.

## SUPPORTING INFORMATION

**How to cite this article:** TJP Bray, GV Minore, A Bainbridge, SA Taylor, MA Hall-Craggs, and H Zhang (2024), RAIDER: Rapid, anatomy-independent deep learning-based chemical shift-encoded MRI, *arXiv*, 2024;00:1–6.